The Astrophysical Journal, 891:158 (12pp), 2020 March 10 https://doi.org/10.3847/1538-4357/ab7379


# The Bimodal Distribution in Exoplanet Radii: Considering Varying Core Compositions and $H_2$ Envelope's Sizes

Darius Modirrousta-Galian[1,2], Daniele Locci[1], and Giuseppina Micela[1]
[1] INAF—Osservatorio Astronomico di Palermo, Piazza del Parlamento 1, I-90134 Palermo, Italy; darius.modirrousta@inaf.it
[2] University of Palermo, Department of Physics and Chemistry, Via Archirafi 36, Palermo, Italy
*Received 2019 October 14; revised 2020 January 28; accepted 2020 February 5; published 2020 March 16*

## Abstract

Several models have been introduced in order to explain the radius distribution in exoplanet radii observed by Fulton et al. with one peak at $\sim 1.3R_\oplus$, the other at $\sim 2.4R_\oplus$, and the minimum at $\sim 1.75R_\oplus$. In this paper we focus on the hypothesis that the exoplanet size distribution is caused by stellar X-ray and ultraviolet (XUV)-induced atmospheric loss. We evolve $10^6$ synthetic exoplanets by exposing them to XUV irradiation from synthetic zero-age main-sequence stars. For each planet we set a different interior composition, which ranged from 100 wt% Fe (very dense), through to 100 wt% $MgSiO_3$ (average density), and to 100 wt% $H_2O$ ice (low density), with varying hydrogen envelope sizes that varied from 0 wt% (a negligible envelope) to 100 wt% (a negligible core). Our simulations were able to replicate the bimodal distribution in exoplanet radii. We argue that in order to reproduce the distribution by Fulton et al. it is mandatory for there to be a paucity of exoplanets with masses above $\sim 8M_\oplus$. Furthermore, our best-fit result predicts an initial flat distribution in exoplanet occurrence for $M_P \lesssim 8M_\oplus$ with a strong deficiency for planets with $\lesssim 3M_\oplus$. Our results are consistent with the $\sim 1.3R_\oplus$ radius peak mostly encompassing denuded exoplanets, while the $\sim 2.4R_\oplus$ radius peak is mainly comprised of exoplanets with large hydrogen envelopes.

*Unified Astronomy Thesaurus concepts:* Exoplanets (498); Super Earths (1655); Mini Neptunes (1063)

## 1. Introduction

Ever since the discovery of the bimodal distribution in exoplanet sizes (Fulton et al. 2017) with one peak at $\sim 1.3R_\oplus$, the other at $\sim 2.4R_\oplus$, and the minimum at $\sim 1.75R_\oplus$, multiple models have been put forward attempting to explain this shape. Although formational mechanisms and arguments have been proposed (e.g., Ginzburg et al. 2016, 2018; Gupta & Schlichting 2018; Zeng et al. 2018), in this paper we will focus on how stellar X-ray and ultraviolet (XUV) irradiation erodes away the primordial $H_2$-dominated atmospheres of exoplanets (e.g., Lecavelier Des Etangs 2007; Ehrenreich & Désert 2011; Lammer et al. 2013; Jin et al. 2014; Jin & Mordasini 2018; Kubyshkina et al. 2018a) and its contribution in shaping the distribution. One of the most highly cited models is Owen & Wu (2013, 2017) which assumes that *Kepler* planets orbiting Sun-like stars have Earth-like interiors, and have masses that vary according to a Rayleigh distribution with a mode at $\sim 3M_\oplus$. According to their model, exoplanets with masses above $\sim 3M_\oplus$ had large $H_2$ atmospheres while planets with masses beneath this threshold were born approximately bare. In this paper we take a different and more general approach to atmospheric mass-loss than Owen & Wu (2013, 2017). Specifically, we account for interiors that range from 100 wt% Fe–100 wt% $H_2O$ that host $H_2$ envelopes. These primordial envelopes will scale from 0 wt% (a negligible or non-existent atmosphere) to 100 wt% (a negligible or non-existent core) of the total mass. We also do not focus on the process through which an exoplanet loses its atmosphere, just the beginning and the end result. By considering the multiplicity of compositions and envelopes we evolve a synthetic population of $10^6$ exoplanets to test whether the bimodal distribution observed by Fulton et al. (2017) could be reproduced.

## 2. Initial Conditions

### 2.1. Stellar Population

As of 2019 September there are ~4000 known exoplanets in total; however, for this study we are only interested in the *Kepler* candidates. To keep in line with Fulton et al. (2017) we only considered planets with orbital periods $\leqslant$100 days. From these we could extract useful stellar information out of 2171 via the NASA Exoplanet Archive. Discarding O-, A-, B-, and F0-F5 type stars (which were only 29 in number) left us with 2142. The resultant distribution of stellar spectral types is shown in Table 1.

Even if this data set is biased due to instrumental limitations, it was used to generate the bimodal distribution by Fulton et al. (2017), so we may use it to generate a synthetic population of $10^6$ zero-age main-sequence stars with their spectral-type distribution corresponding to Table 1 and their masses, radii, and temperatures matching those predicted by Siess et al. (2000; see Table 2). We are aware that stars evolve with age but since most of the XUV-induced evaporation occurs within the first ~1 Gyr we can ignore this evolution and instead focus on the irradiation present during the star's youth. We also did not account for small variations within each spectral class of mass, radius, metallicity, and temperature since the effects on our final results would be negligible.

In order to estimate the frequency of each sub-type we divided the frequency of each spectral class by the number of sub-types given by Siess et al. (2000; see Table 2). Regarding the XUV stellar irradiation, we used the equations by Penz & Micela (2008) for M-type stars and Penz et al. (2008) for G-type stars with the UV fluxes from Sanz-Forcada et al. (2011). Since K-type stars are intermediate in X-ray luminosity levels we set their values as being inbetween M- and G-types. For late F-type stars we set their XUV luminosities as equivalent to G0-type stars which is adequate for our statistical model.

**Table 1**
Stellar Spectral-type Frequency for Known Exoplanets with Orbital Periods ⩽100 Days

| Type | Number | Norm. Fraction (%) |
|---|---|---|
| M | 14 | 0.654 |
| K | 376 | 17.554 |
| G | 1311 | 61.204 |
| F (F5-F9) | 441 | 20.588 |

**Note.** Data from the NASA Exoplanet Archive.

**Table 2**
The Properties of Our Synthetic Population Siess et al. (2000)

| Type | Mass ($M_*$) | Radius ($R_*$) | Temperature (K) |
|---|---|---|---|
| M6 | 0.1 | 0.192 | 2973 |
| M5 | 0.2 | 0.224 | 3244 |
| M3 | 0.3 | 0.299 | 3474 |
| M2 | 0.4 | 0.360 | 3654 |
| M1 | 0.5 | 0.430 | 3811 |
| M0 | 0.6 | 0.517 | 3982 |
| K6 | 0.7 | 0.623 | 4261 |
| K4 | 0.8 | 0.735 | 4617 |
| K2 | 0.9 | 0.850 | 4925 |
| K1 | 1.0 | 0.965 | 5239 |
| G9 | 1.1 | 1.110 | 5475 |
| G7 | 1.2 | 1.290 | 5685 |
| G2 | 1.3 | 1.450 | 5917 |
| F9 | 1.4 | 1.640 | 6116 |
| F7 | 1.5 | 1.840 | 6296 |
| F5 | 1.6 | 2.030 | 6489 |

### 2.2. Orbital Parameters

When we plot the planetary radii versus the semimajor axis distances, a deficit of bodies intermediate in size between a super-Earth and a sub-Jupiter with short orbital periods (see Figure 1) can be seen. This paucity is believed to be due to the photoevaporation of primordial atmospheres (e.g., Owen & Lai 2018). Since our code will evolve synthetic exoplanets from before the time that their atmospheres were eroded, we will assume that there was no gap straight after their formation, so a planet with an arbitrary radius could have any arbitrary orbital distance. Notwithstanding, we set an upper limit for the radius of our synthetic exoplanets at $R_{\rm P} \approx 8.0 R_{\oplus}$ (i.e., $M \approx 25 M_{\oplus}$ for a cold $H_2$ body) in order to exclude Saturn- and Jupiter-mass planets, which are more resilient to atmospheric erosion. With this assumption it became possible to begin sampling exoplanetary orbital distances. The histogram of the semimajor axial distances showed that the average orbit is at ∼0.1 au (see Figure 2). This distribution was best fit by a lognormal curve between a minimum distance set by the Roche limit (Aggarwal & Oberbeck 1974) of each individual star and a maximum distance corresponding to a period of 100 days. We approximated the Roche limits of the stars as $\sim 2R_*$, where $R_*$ is the radius of the host star being considered at that moment, because planets with large $H_2$ envelopes, such as the outer planets in our solar system, have stellar-like densities. This approximation breaks down for exoplanets born with very small atmospheres but these should be scarce since most planets are thought to begin with large $H_2$ repositories (e.g., Hayashi et al. 1985; Ikoma & Hori 2012).

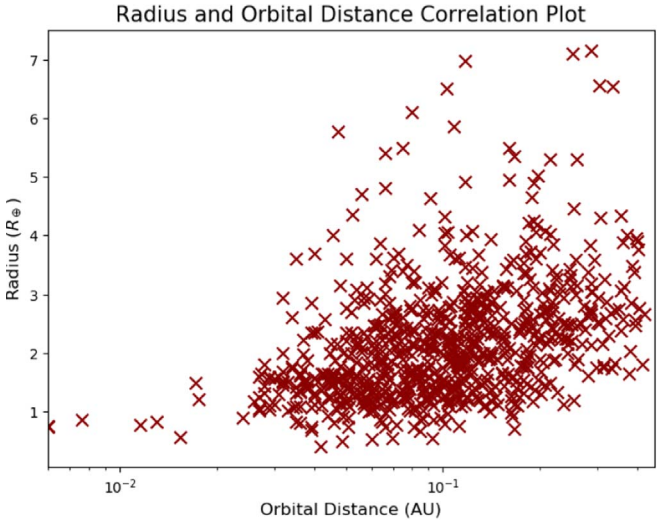


**Figure 1.** Semimajor axial distance (au) plotted against planetary radius ($R_{\oplus}$) for orbital periods ⩽100 days. 787 data points, all of which were collected on 2019 September from the NASA Exoplanet Archive.

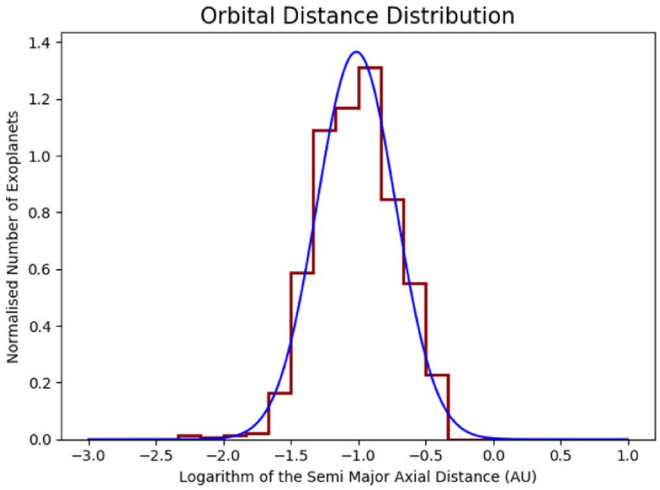


**Figure 2.** Normalized observed distribution of exoplanet orbital distances (red) and the lognormal approximation (blue) for exoplanets with orbital periods ⩽100 days. 838 data points, all of which were collected on 2019 September from the NASA Exoplanet Archive.

### 2.3. Planetary Parameters

Our initial population of exoplanets was modeled as having $H_2$ atmospheres so their average densities had to be lower than a purely silicate planet. However, it is possible that some exoplanets formed with very small or non-existent atmospheres while others formed almost entirely as hydrogen spheres with no core. Consequently, we modeled the variation in exoplanet radii with a laplace distribution where for each planet the maximum allowed density was set as a 100 wt% Fe sphere, the minimum density was modeled as a 100 wt% $H_2$ sphere, and the average density was given by a terran core with a $H_2$-rich atmosphere. For the Fe and terran mass–radius models we approximated the numerical data in Zeng & Sasselov (2013) and Zeng et al. (2016) with a best-fit curve, while for the pure hydrogen planet we used Becker et al. (2014). Figure 3 shows the mass and radius relation of 500 synthetic exoplanets as given by our laplace distribution.

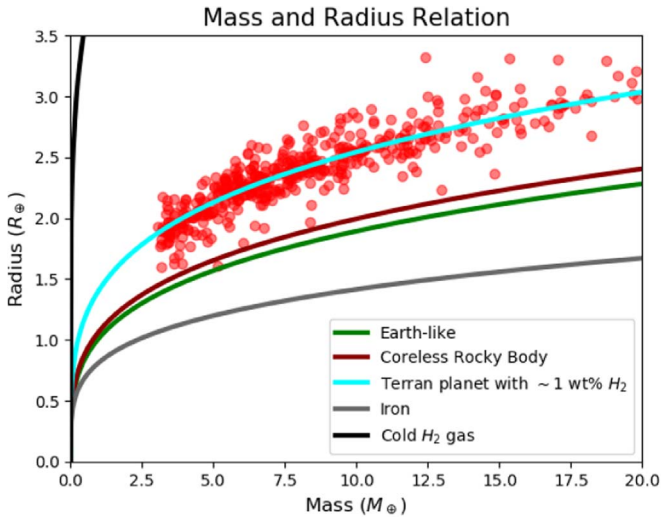


**Figure 3.** Mass and radius distribution of 500 of our synthetic exoplanets before undergoing photoevaporation. All mass and radius curves come from Zeng & Sasselov (2013) and Zeng et al. (2016) except for the cold $H_2$ curve, which originated from the equations of state by Becker et al. (2014) that were then adapted by Zeng et al. (2018). The radius distribution was given by a laplacian function with a mean corresponding to a terran planet with 1 wt% $H_2$ envelope and a scale parameter of 0.10 (i.e., a standard deviation of $\sqrt{2}/10$). The reason for the lack of planets with $M_P < 3M_\oplus$ is explained later in the manuscript.

100 wt% Fe planet radius (Zeng & Sasselov 2013; Zeng et al. 2016):

$$\frac{R_{\rm Fe}}{R_\oplus} = 0.815 \times \left(\frac{M_P}{M_\oplus}\right)^{1/4.176}. \quad (1a)$$

Terran planet with ~1 wt% $H_2$-rich envelope radius (Zeng & Sasselov 2013; Zeng et al. 2016):

$$\frac{R_{\rm Rock+H_2}}{R_\oplus} = 1.410 \times \left(\frac{M_P}{M_\oplus}\right)^{1/3.905}. \quad (1b)$$

100 wt% $H_2$ planet radius (Becker et al. 2014; Zeng et al. 2018):

$$\frac{R_{\rm H_2}}{R_\oplus} = 4.106 \times \left(\frac{M_P}{M_\oplus}\right)^{1/5.010}, \quad (1c)$$

where $M_P$ is the planetary mass in kg, $M_\oplus$ is Earth's mass in kg, and $R_\oplus$ is Earth's radius in m. Regarding the planetary mass, we have very few measurements for super-Earths and sub-Neptunes, and even when we do have values they sometimes suffer from large uncertainties. Because of this, we have very strong observational biases toward larger masses (e.g., Howard et al. 2010; Marcy et al. 2014; Malhotra 2015) which means that as of now it is not possible to accurately and reliably know the mass function of exoplanets. Consequently, we will set the initial planetary mass distribution as a variable which we will manually adjust in order match the observed radius gap as given by Fulton et al. (2017).

Some planets are young enough that their atmospheres are still extant despite strong irradiation that would, in the future, denude the planet. These bodies are younger than the amount of time required for their complete atmospheric loss. Using the age of their host stars, which is given by the NASA Exoplanet

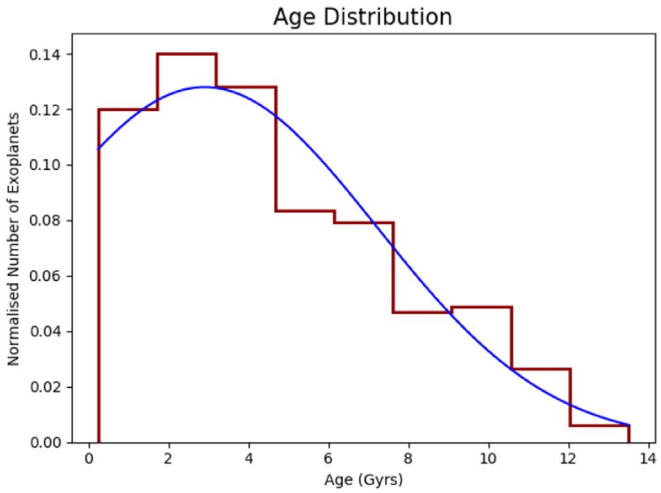


**Figure 4.** Observed normalized distribution of exoplanet ages (red) and the truncated Gaussian approximation (blue) for orbital periods ⩽100 days. All 341 data points were collected on 2019 September from the NASA Exoplanet Archive. We only used *Kepler* candidates.

Archive as proxies, the age distribution of exoplanets is best described by a truncated Gaussian with a mean of ~2.9 Gyr, standard deviation of ~4.3 Gyr, and a minimum and maximum age of ~0.25 Gyr and ~13.5 Gyr, respectively (shown in Figure 4). It is important to note that the age of the stars cannot be directly measured and it is calculated using theoretical modeling, which is known to be uncertain. However, it is beyond the scope of this study to do an in-depth analysis of these models.

With regards to the mass-loss timescale, for a super-Earth or sub-Neptune this is approximated by:

$$t_{\rm mass\ loss} \sim \frac{M_{\rm env}}{\dot{M}_{\rm env}}, \quad (2a)$$

where

$$M_{\rm env} = \begin{cases} 0.01 M_P & \text{if } M_P < \Upsilon_\alpha \\ M_P - \Gamma_\beta & \text{if } \Upsilon_\alpha \leqslant M_P < \Upsilon_\beta, \\ M_P - \Gamma_\gamma & \text{if } M_P \geqslant \Upsilon_\beta \end{cases} \quad (2b)$$

where $M_{\rm env}$ is the mass of the primordial envelope, and $\dot{M}_{\rm env}$ is the hydro-based mass-loss rate, which is described in Kubyshkina et al. (2018b). Since in our study we only focused on the beginning and end result of the mass-loss evolution, we could not include the time dependence on the XUV flux rate. Therefore, in order not to make an overestimation (e.g., by assuming a constant initial flux throughout the lifetime of the star), we modeled this parameter as a step function where $F_{\rm XUV} = F_0$ from 0 to 1 Gyr and $F_{\rm XUV} = 0$ for >1 Gyr. The initial flux $F_0$ was adopted from Penz & Micela 2008, Penz et al. 2008, and Sanz-Forcada et al. 2011. In addition, the treatment of the flux as a step function is consistent with these studies as during the first billion years of a stars' life the XUV flux is approximately constant, with it then quickly decaying by several orders of magnitude. In Figures 5 and 6 we show how this approximation is adequate. Regarding $\Upsilon_\alpha$ and $\Upsilon_\beta$, these are the critical masses that separate the different regimes $\alpha$, $\beta$, and $\gamma$. $\Gamma_\beta$ and $\Gamma_\gamma$ are probabilistic functions with ranges between $\Upsilon_\alpha - M_P$ and $\Upsilon_\beta - M_P$, respectively. When $\Gamma_{\beta\ {\rm or}\ \gamma} = M_P$ this

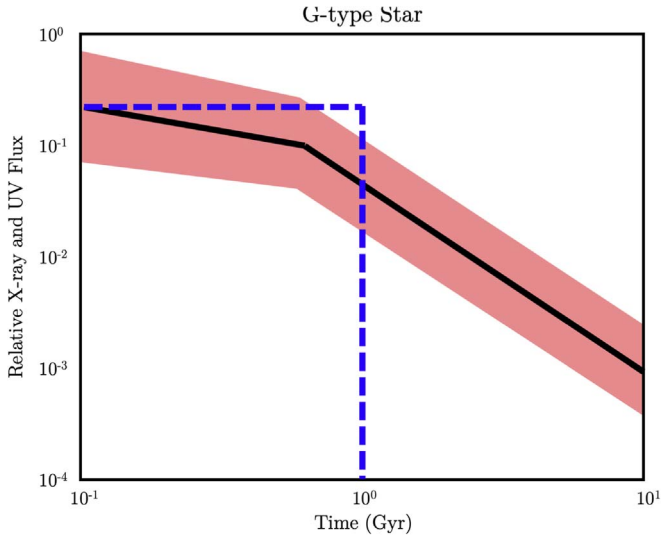


**Figure 5.** Relative XUV flux of G-type stars. The red shaded region marks the measurements from Penz et al. (2008) and Sanz-Forcada et al. (2011). The black line is the average measured XUV flux. The blue dashed line shows the step function we adopted in our model.

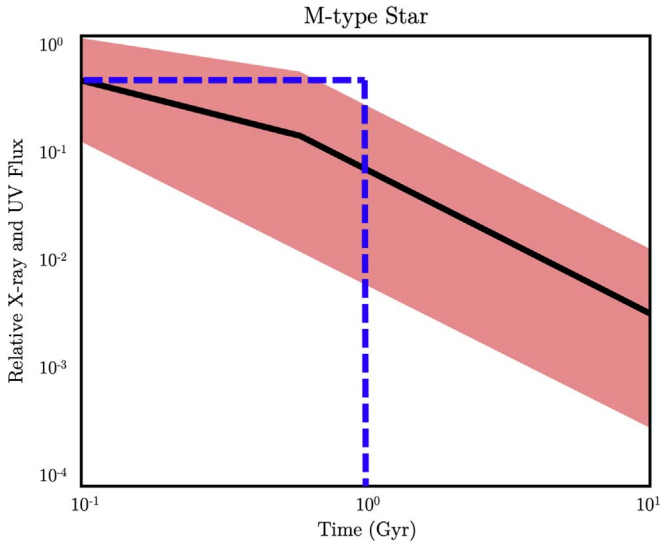


**Figure 6.** Relative XUV flux of M-type stars. The red shaded region marks the measurements from Penz & Micela (2008) and Sanz-Forcada et al. (2011). The black line is the average measured XUV flux. The blue dashed line shows the step function we adopted in our model.

implies that the planetary envelope is non-existent, while if $\Gamma_\beta = \Upsilon_\alpha$ or $\Gamma_\gamma = \Upsilon_\beta$ are for the cases when the planet has the minimum core mass required to be in that specific region:

1. $\alpha$ marks the region where smaller planets typically accrete hydrogen envelopes that are $\sim$1% of the total planetary mass (e.g., Stevenson 1999; Ikoma & Hori 2012; Chachan & Stevenson 2018). This region will be within the mass limits of $0 - \Upsilon_\alpha$.
2. $\beta$ is where planets have enough mass to accrete larger envelopes but the cores are still not massive enough to form Neptunian- or Jupiter-mass bodies (e.g., Ikoma & Hori 2012; Chachan & Stevenson 2018). Region $\beta$ will be within the mass limits of $\Upsilon_\alpha$ and $\Upsilon_\beta$.
3. In the $\gamma$ region planets undergo runaway gas accretion. This implies that generally any extra mass above the critical mass $\Upsilon_\beta$ will mostly be due to hydrogen gas. Typically, theoretical models predict that the critical mass $\Upsilon_\beta \sim 10M_\oplus$ (e.g., Ida & Lin 2004, 2005, 2008; Mordasini et al. 2009). However, as systems undergo runaway growth, planetesimals are also accreted which could increase the mass of the core (Shiraishi & Ida 2008; Shibata & Ikoma 2019). This extra growth of the core needs to be balanced with the core erosion induced from deposited energy but the latter effect is believed to be inefficient (Moll et al. 2017). In addition, internal models of the gaseous planets in our solar system predict core masses in the range of 7–25$M_\oplus$ (e.g., Mizuno 1980; Stevenson 1982; Hubbard & Marley 1989; Chabrier et al. 1992; Guillot et al. 1997; Gudkova & Zharkov 1999; Guillot 1999; Wahl et al. 2017). Therefore, the remnant cores of Neptunian or Jovian planets could be $>10M_\oplus$. The possibility of very heavy cores is also supported by the discovery of rocky mega-Earths such as BD+20594 b, which has a mass and radius of $16.3 \pm 6.0M_\oplus$ and $2.2 \pm 0.1R_\oplus$ (Espinoza et al. 2016) or K2-66 b with $21.3 \pm 3.6M_\oplus$ and $2.50 \pm 0.3R_\oplus$ (Sinukoff et al. 2017), respectively. Therefore, while the critical mass $\Upsilon_\beta \sim 10M_\oplus$, the probabilistic function $\Gamma_\gamma$ could range from 10 to $25M_\oplus$ according to observations and theoretical predictions.

Having considered all of the above, we will adjust our input distributions for $\Gamma_\beta$ and $\Gamma_\gamma$ and our critical masses $\Upsilon_\alpha$ and $\Upsilon_\beta$ in order to find a best-fit radius distribution.

## 3. Evolution Model

The simplest summary of our model is that our synthetic exoplanets travel one of three evolutionary paths:

1. The exoplanet is younger than its mass-loss timescale so it currently maintains its envelope.
2. The exoplanet has the right orbital and physical properties required for its primordial envelope to outlive its host star's lifetime (Locci et al. 2019).
3. The exoplanet loses its atmosphere before undergoing any counter-mechanism.

In our code we integrated an algorithm (see Figure 7) that implemented the above points. Now that we knew each evolutionary path, we needed to model each step accordingly.

### 3.1. First Path

If the age of the planet is less than the mass-loss timescale, we did not evolve it (see Equation (3)). However, if the contrary is true we moved it to the next stage.

$$t_{\text{age}} < t_{\text{mass loss}}. \quad (3)$$

### 3.2. Second Path

The second path is concerned with whether the initial mass of an exoplanet's envelope is large enough to survive the incident XUV irradiation for the remainder of the host star's life. In order to estimate this minimum survivable mass, we first calculated the mass-loss rate for different synthetic giant exoplanets. To do this we adapted the numerical model for the mass-loss rate described in Locci et al. (2019). This model calculates the mass-loss rate using the "energy-limited approach" that was first proposed by Watson et al. (1981) and was later revisited by Erkaev et al. (2007). We then

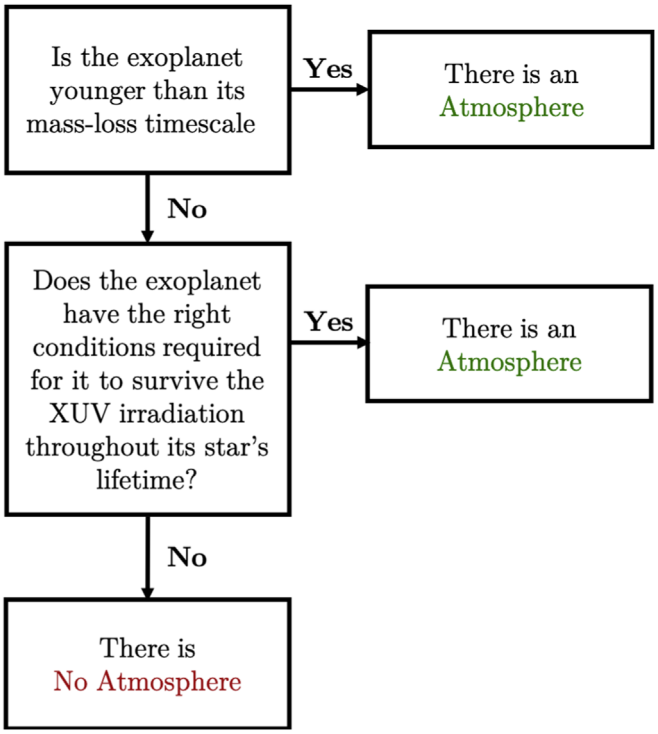


**Figure 7.** Flowchart showing the path our code took when evolving the exoplanets.

performed a temporal evolution of the synthetic gaseous planet population, where at each arbitrary unit of time we:

1. Calculated the mass-loss rate.
2. Updated the total planetary mass.
3. Updated the planetary radius accounting for both mass lost and gravitational shrinking (see Locci et al. 2019, for details).

For the duration of the simulation, we adopted:

1. An average G-type lifetime of 10 Gyr.
2. Different possible exoplanet orbital distances.
3. Varying initial X-ray luminosities of the parent star.

After the evolution we took note of the planets that ended up as super-Earths, from which we then retrieved their initial masses for their given distances and stellar X-ray luminosities. When a planet ended its evolution with a mass less than $2.6M_{\oplus}$, we defined it as having lost all of its gaseous envelope. We chose $2.6M_{\oplus}$, as according to the mass–radius relations of Zeng & Sasselov (2013) and Zeng et al. (2016) this would correspond to a rocky planet with a radius at $\sim 1.3R_{\oplus}$, which according to Fulton et al. (2017) is located at the first peak of the radius distribution. If the planet instead has a hydrogen envelope with a total combined mass of $2.6M_{\oplus}$, its radius would be $\sim 1.8R_{\oplus}$, which is located within the Fulton gap. Consequently, this mass threshold implies that planets originally located within the region of the radius gap lost their envelopes to "fill-up" the first peak at $\sim 1.3R_{\oplus}$.

We also accounted for the fact that luminosities evolve with time, as described in Penz et al. (2008) and Penz & Micela (2008). Finally, using this procedure, we retrieved the initial mass thresholds as functions of the orbital distance, for different stellar luminosities, and for M- and G-type stars (in Figures 8 and 9 we show the mass threshold functions for a G-type and M-type star,

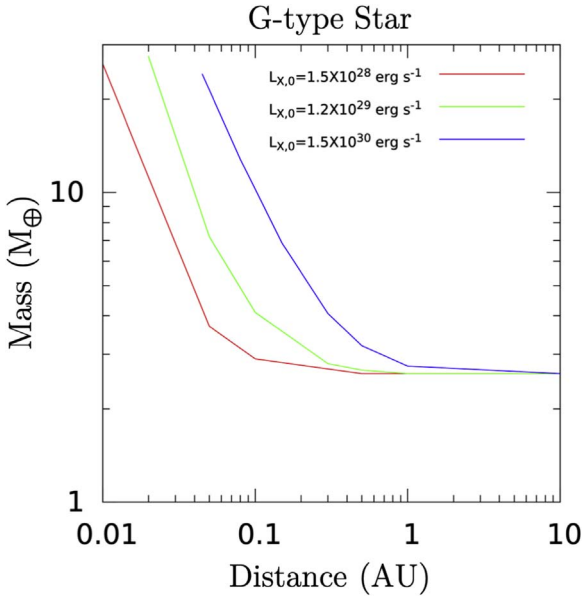


**Figure 8.** Mass threshold functions calculated using the model from Locci et al. (2019) for G-type stars for different initial X-ray luminosities (Penz et al. 2008). The UV luminosities scale with the X-ray ones according to the models by Sanz-Forcada et al. (2011).

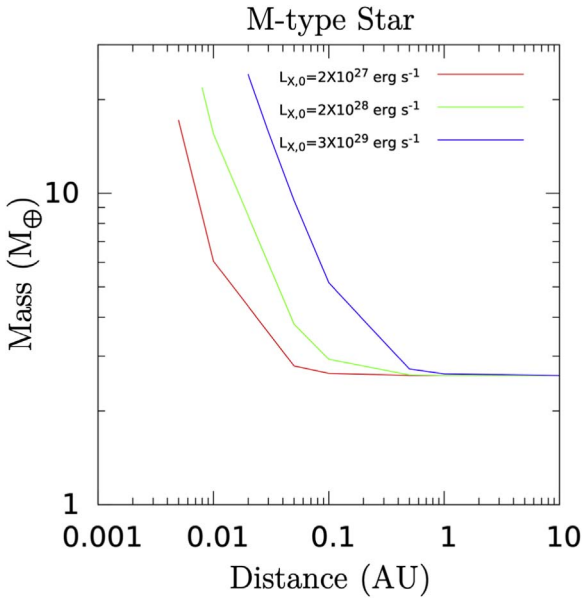


**Figure 9.** Mass threshold functions calculated using the model from Locci et al. (2019) for M-type stars for different initial X-ray luminosities (Penz & Micela 2008). The UV luminosities scale with the X-ray ones according to the models by Sanz-Forcada et al. (2011).

respectively, for given initial X-ray luminosities). These are the mass limits required for an exoplanet with a certain mass and radius to survive its host stars XUV irradiation throughout its lifetime. During our exoplanet simulations around their host stars we occasionally interpolated between the calculated values of the minimum mass in order to obtain a best-fit curve for each given luminosity.

### 3.3. Third Path

If an exoplanet makes it to the third stage, it will lose its hydrogen atmosphere. In order to model this, we subtracted the

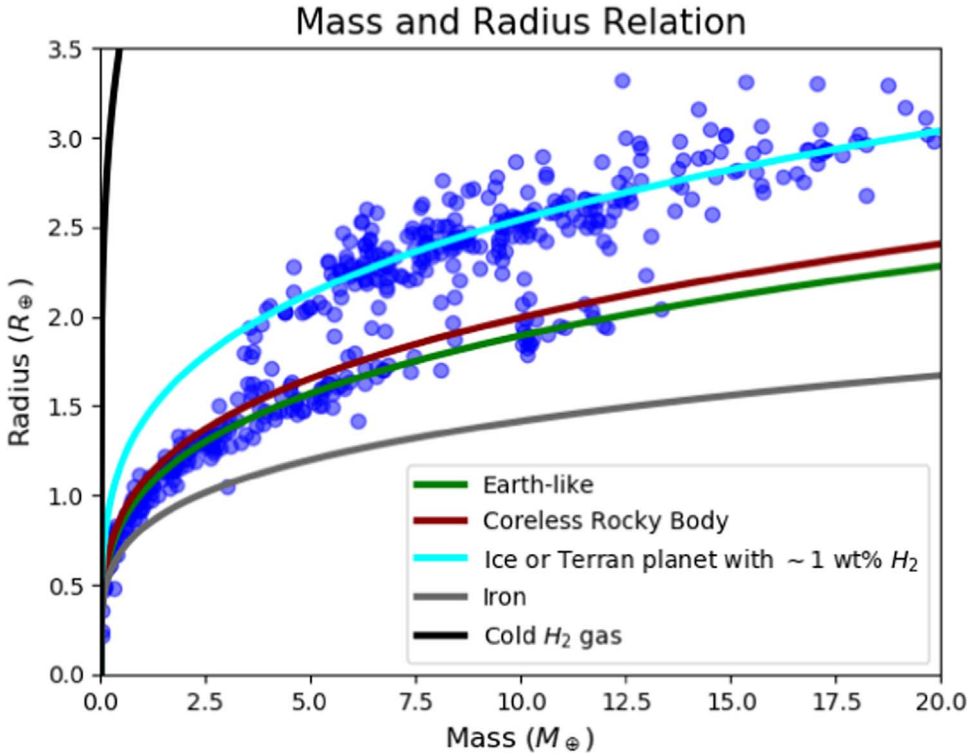


**Figure 10.** Mass and radius distribution of 500 of our synthetic exoplanets after undergoing photoevaporation. All mass and radius curves come from Zeng & Sasselov (2013) and Zeng et al. (2016) except for the cold $H_2$ curve which originated from the equations of state by Becker et al. (2014) that were then adapted by Zeng et al. (2018). The scale parameter of the laplacian function of the radii was set to 0.05 (i.e., a standard deviation of $\sqrt{2}/20$).

atmospheric mass (given in Equation (2b)) from the total planetary mass ($M_P$). Once the masses had been reduced we then calculated their corresponding radii. Since these planets would lack hydrogen atmospheres, their minimum possible densities were consistent with 100% $H_2O$ ice planets (Zeng & Sasselov 2013; Zeng et al. 2016), while their maximum possible densities were given by the remnant cores of evaporated Neptunian or Jovian planets (Mocquet et al. 2014). The mean density of our evolved planets was set to an Earth-like silicate planet with a core comprising 30% of the total mass (Zeng et al. 2016). We distributed the occurrence of each of these compositions according to a laplacian distribution, which is shown in Figure 10.

Gas giant or Neptunian remnant core (Mocquet et al. 2014):

$$\frac{R_{\text{Remnant Core}}}{R_\oplus} = 0.469 \times \left(\frac{M_P}{M_\oplus}\right)^{1/3}. \quad (4a)$$

Terran planet with no atmosphere (Zeng & Sasselov 2013; Zeng et al. 2016):

$$\frac{R_{\text{Rock}}}{R_\oplus} = 1.007 \times \left(\frac{M_P}{M_\oplus}\right)^{1/3.7}. \quad (4b)$$

100% $H_2O$ planet radius (Zeng & Sasselov 2013; Zeng et al. 2016):

$$\frac{R_{H_2O}}{R_\oplus} = 1.410 \times \left(\frac{M_P}{M_\oplus}\right)^{1/3.905}. \quad (4c)$$

However, if the original (pre-evolution) planetary density was already higher than an Earth-like silicate planet, we also sampled its new radius with a laplace distribution, but between the limits set by its pre-evolution radius and the radius of a remnant gas giant/Neptunian core. The mean of the distribution was also set at its pre-evolution radius (see Table 3 for more details). Nevertheless, the majority of newly formed planets are expected to have densities lower than purely silicate bodies due their primordial envelopes. Consequently, the contribution from these rare exoplanets is expected to be negligible.

Comparing Figures 10 with 3 shows the expected XUV-irradiation-induced evolution in the mass–radius curves of exoplanets. While the original mass and radius plot is centered around the ice or rocky planet with $H_2$ envelope line, the second plot shows signs of two separate compositions. These being the original low-mass, low-density planets, and rocky worlds. A small gap can also be distinguished between the ice/terran planet with a $H_2$ envelope line and the Earth-like composition line. Figure 10 follows a similar trend to the mass and radius plot of real exoplanets as shown in Figure 2 of Zeng et al. (2018).

## 4. Results

After evolving $10^6$ exoplanets we are able to replicate the observed bimodal distribution in exoplanet radii with one peak at $\sim 1.3 R_\oplus$, the other at $\sim 2.4 R_\oplus$, and the minimum at $\sim 1.75 R_\oplus$ (see Figure 11). Our results matched well with the observations by Fulton et al. (2017) while also being consistent with the presence of the sub-Jovian desert (e.g., Owen & Lai 2018) (see Figures 1 and 12). Furthermore, our final radius distribution is within the error bars given by the data points in Table 3 and Figure 7 of Fulton et al. (2017). Our model predicts that, initially, most exoplanets were centered around a peak of $\sim 2.4 R_\oplus$ that decayed in a laplacian manner, as shown in Figure 11. In order to achieve the bimodal behavior we found that it was mandatory for there to

**Table 3**
Adopted Input Distributions

| Exoplanet Property | Functional Form | Parameters |
|---|---|---|
| Orbital Distance | Lognormal | • Max = 100 days<br>• Min = $R_{\rm Roche} \sim 2R_*$<br>• $\mu \approx -1$<br>• $\sigma \approx 0.3$ |
| Initial Mass | $=\begin{cases}\text{Uniform} & 3M_\oplus \leqslant M_{\rm P} < 8M_\oplus \\ \text{Pareto} & 8M_\oplus \leqslant M_{\rm P} \leqslant 25M_\oplus\end{cases}$ | Pareto<br>• $Mo = 8.0M_\oplus$<br>• $a = 1.6$ |
| Initial Compositions | Laplace | • Max = Equation (1c)<br>• Min = Equation (1a)<br>• $\mu$ = Equation (1b)<br>• $b = \sqrt{2}\sigma = 0.1R_\oplus$ |
| Ages | Trunc. Normal | • Max = 13.51 Gyr<br>• Min = 0.25 Gyr<br>• $\mu \approx 2.9$ Gyr<br>• $\sigma = 4.3$ Gyr |
| $\Gamma_\beta$ (Equation (2b)) | Uniform | • Max = $M_{\rm P}$<br>• Min = 0 |
| $\Gamma_\gamma$ (Equation (2b)) | Pareto | • Max = $M_{\rm P}$<br>•Min = 0<br>• $Mo = 10M_\oplus$<br>• $a = 1$ |
| Final Compositions | Laplace | $R_{\rm Initial} >$ Equation(4b)<br>• Max = Equation (4c)<br>• Min = Equation (4a)<br>• $\mu$ = Equation (4b)<br>• $b = \sqrt{2}\sigma = 0.05R_\oplus$<br>$R_{\rm Initial} <$ Equation(4b)<br>• Max = $R_{\rm Initial}$<br>• Min = Equation (4a)<br>• $\mu = R_{\rm Initial}$<br>• $b = \sqrt{2}\sigma = 0.05R_\oplus$ |

**Note.** Mo = Mode, $\mu$ = arithmetic mean, $\sigma$ = standard deviation, $a$ = shape, $b$ = scale, Max and Min are the maximum and minimum limits respectively.

be a paucity of exoplanets $\gtrsim 8M_\oplus$ (see Figure 13). For best results we found that this region should be preceded by a flat distribution between 3 and $8M_\oplus$ and another paucity for planets $\lesssim 3M_\oplus$. Because our best-fit initial mass distribution has a lack of planets with $\lesssim 3M_\oplus$, we predict that within the confines of our observations, bodies situated in section $\alpha$ of Equation (2b) should be absent or in the very least relatively scarce. With respect to the initial hydrogen envelope masses in Equation (2b), we find best-fit critical masses of $\Upsilon_\alpha = 3{\rm M}_\oplus$, $\Upsilon_\beta = 10M_\oplus$ with the probabilistic functions $\Gamma_\beta$ and $\Gamma_\gamma$ detailed in Table 3.

Regarding the final mass distribution (see Figure 13), for masses greater than $\sim 11.5M_\oplus$, the difference between the initial and final distribution is very small. This is because with bigger masses it becomes exceedingly harder to remove the primordial hydrogen envelopes of exoplanets due to their stronger gravitational strengths. From 10 to $11.5M_\oplus$ we predict a small increase in the abundance that is caused by the remnant cores of Neptunian or Jovian planets (more details on this can be found in Section 5). From 3 to $10M_\oplus$ there is a strong decrease in the mass abundance, which is caused by planets with cores $\lesssim 3M_\oplus$ losing the entirety of their envelopes. After the XUV-induced evolution of these planets, the increase in the number of bodies with $\lesssim 3M_\oplus$ corresponds with the radius peak at $\sim 1.3R_\oplus$ (Zeng & Sasselov 2013; Zeng et al. 2016). In spite of the increase in rocky worlds with masses at $\sim 10M_\oplus$ matching the small peak at $1.95R_\oplus$ (despite the uncertainties being large, this is consistent with the $1.77–1.97R_\oplus$ abundance measured by Fulton et al. (2017)), the overall number of planets with radii of $\sim 1.95R_\oplus$ has decreased. This is because despite the increase in rocky cores at $\sim 1.95R_\oplus$, planets with hydrogen envelopes previously located in this region decreased more numerously. Concerning the radius peak at $\sim 2.4R_\oplus$, this is compatible with rocky planets sustaining hydrogen envelopes where the combined total mass is $\sim 8M_\oplus$. According to Zeng & Sasselov (2013) and Zeng et al. (2016), an airless rocky planet with the same mass would instead be located at $\sim 1.8R_\oplus$, which lies in the region of the remnant Neptunian and Jovian cores explained above. With respect to the density evolution, our simulation shows that on average the planet densities increased sharply, which can be seen in Figure 14. Numerically, our results can be summarized as follows with the best-fit input distributions shown in Table 3:

1. ∼1% of known exoplanets are currently in the processes of losing their atmospheres (first path).
2. ∼51% of exoplanets have the right orbital and physical properties required in order for their primordial envelopes to outlive their host star's lifetime (second path).
3. ∼48% of exoplanets completely lost their primordial hydrogen envelopes (third path).

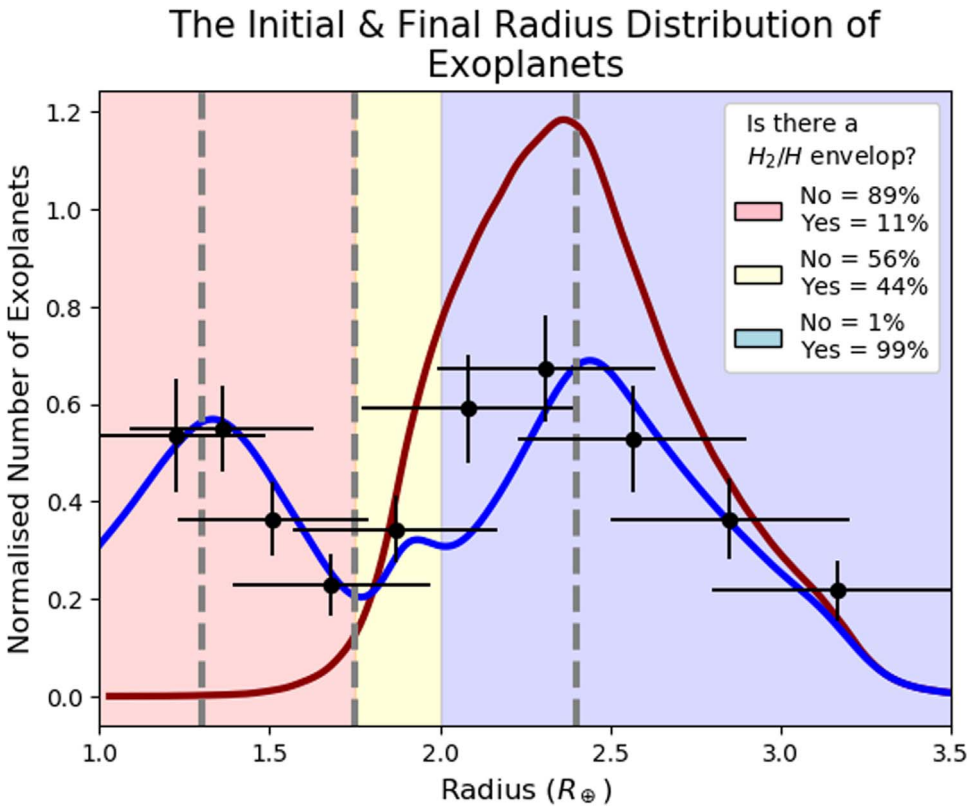


**Figure 11.** Final (blue line) and initial (red line) distributions of exoplanet radii for periods $\leqslant$100 days obtained by our model. The gray lines show the two peaks and the minimum discovered by Fulton et al. (2017). The data points with the uncertainties correspond to the values given in Table 3 and Figure 7 of Fulton et al. (2017). The light-red, light-yellow, and light-blue regions correspond only to the final radius distribution's rocky first peak, the remnant core (mega-Earth)-rich region, and the hydrogen-rich worlds of the second peak, respectively. For each region we report the planet population composition.

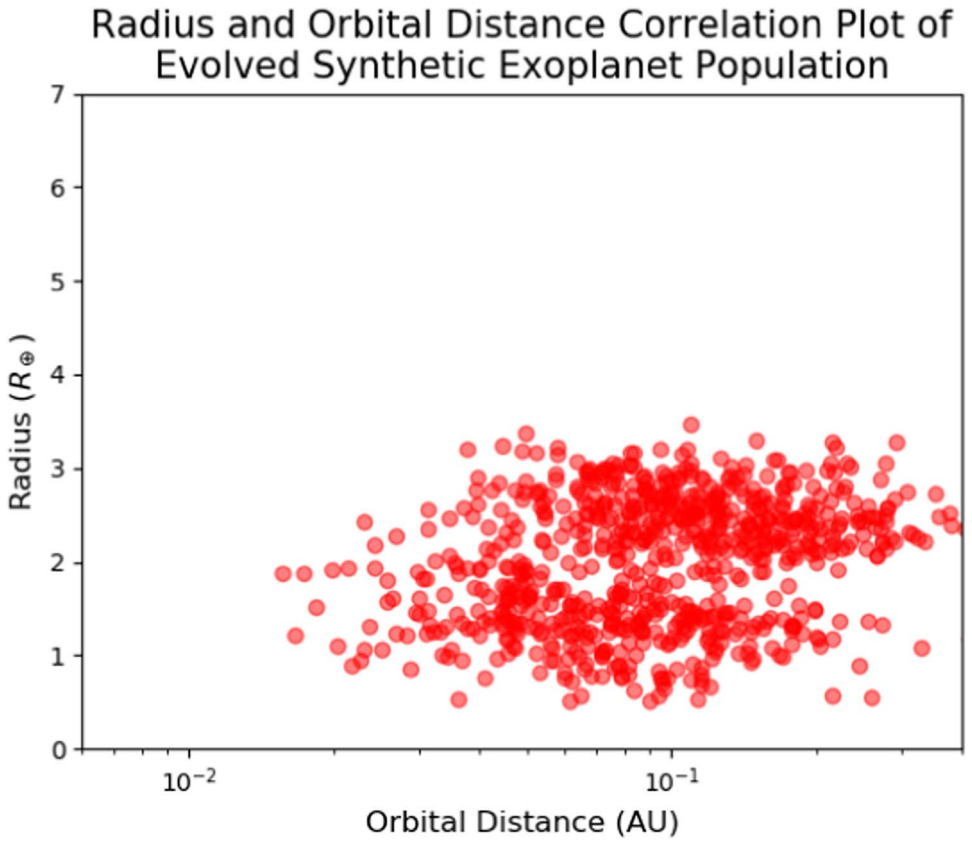


**Figure 12.** A plot of the radius and orbital distance of 787 (for comparison with Figure 1) randomly chosen exoplanets.

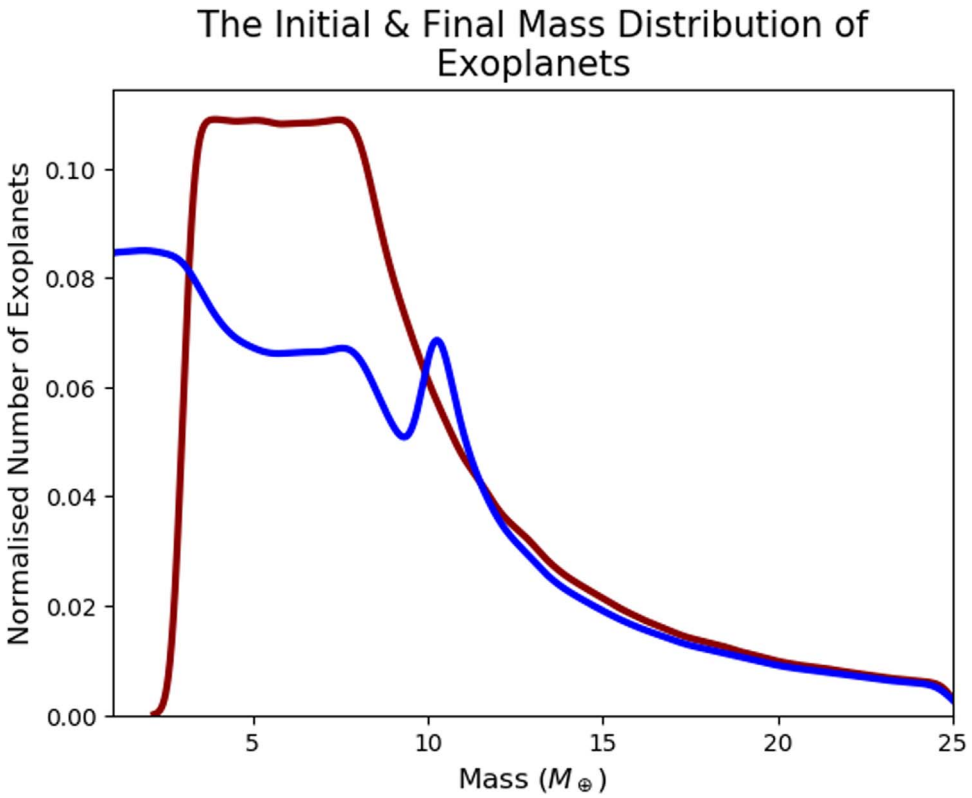


**Figure 13.** Predicted final (blue) and initial (red) mass distributions of exoplanets whose current radii are distributed according to Figure 11. All planets have periods $\leqslant$100 days.

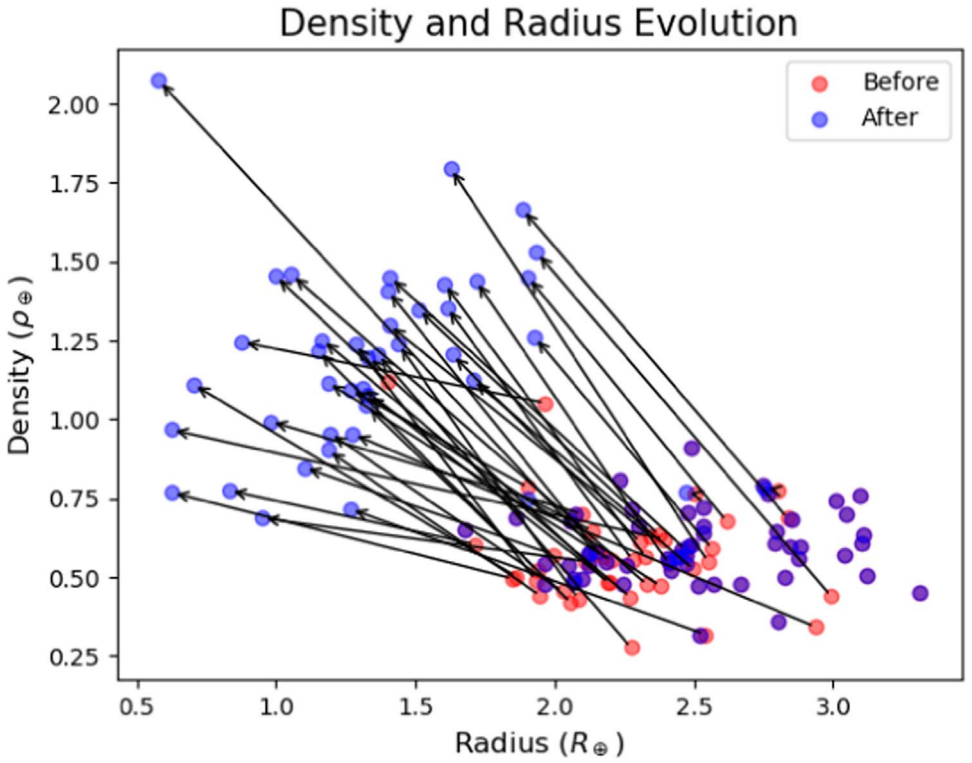


**Figure 14.** A plot showing the density and radius evolution of 100 randomly chosen exoplanets.

## 5. Discussions

Overall, our results are similar to those of Owen & Wu (2013, 2017) where the observed radial distribution was caused due to stellar XUV irradiation triggering atmospheric erosion. However, the differences are due to us adopting the core compositional models of Zeng & Sasselov (2013), Zeng et al. (2016), and Mocquet et al. (2014), which use considerably

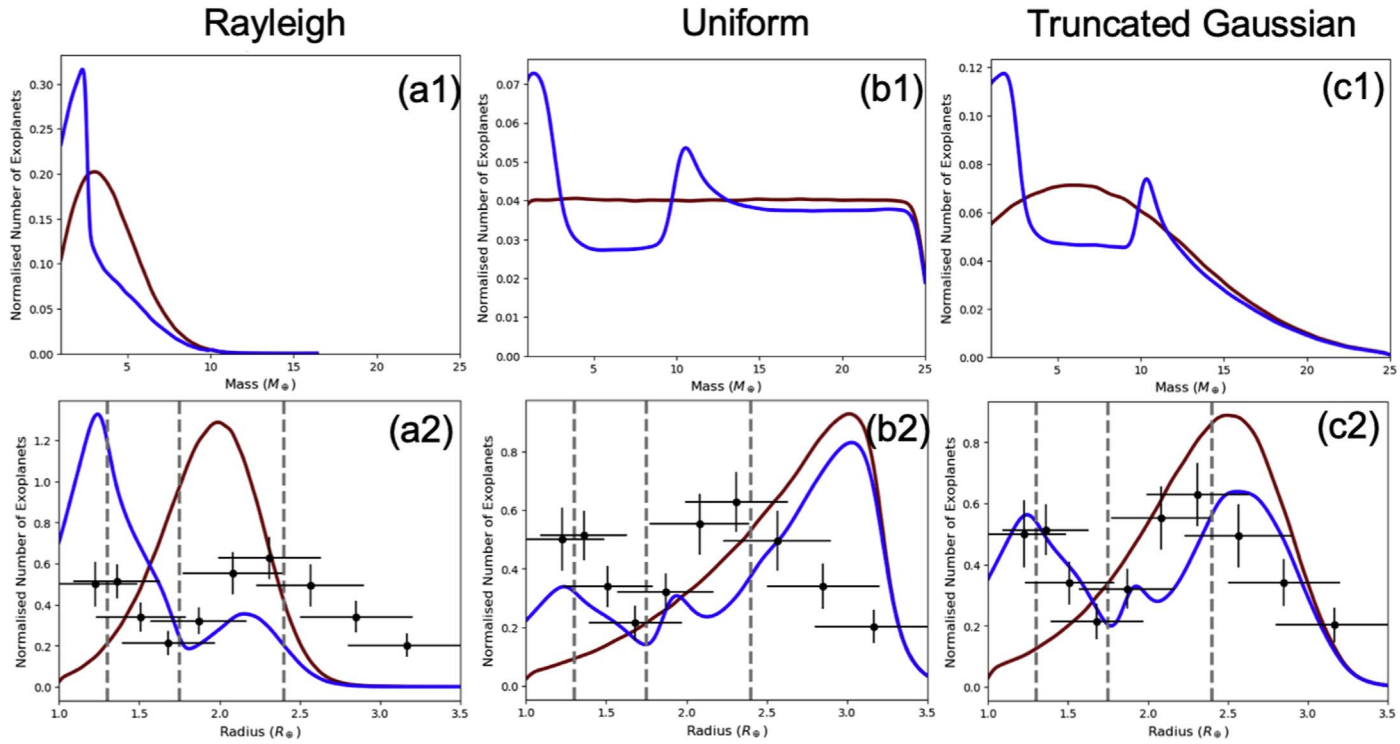


**Figure 15.** A plot showing the initial (red) and final (blue) mass (a1, b1, c1) and radius (a2, b2, c2) functions. The truncated Gaussian function for the mass distribution (c1) has a mean of $6M_\oplus$, a standard deviation of $7M_\oplus$, and a minimum and maximum limit of 0.1 and $25M_\oplus$, respectively.

different equations of state. Our code also predicts a small but non-negligible contribution from large remnant cores (i.e., mega-Earths) formed from the removal of large hydrogen atmospheres from Neptunian-planets. We argue that most of these remnant cores are of mass $\sim 10M_\oplus$, which for decompressed relaxed cores (which occurs after ~few Gyr) corresponds to radii within the range 1.77–$1.97R_\oplus$. This result is compatible with Swain et al. (2019) who identified a "transition region" rich in terrestrial and hydrogen-bearing planets between 1.5 and $2.0R_\oplus$. As explained in Section 2.3 some remnant cores may be much larger, which is corroborated by observational evidence and a strong theoretical foundation. These larger mega-Earths have radii that are located within the $\sim 2.4R_\oplus$ peak implying that this larger peak is dominated by planets with large hydrogen envelopes (~99%) with a few massive mega-Earths (~1%).

Regarding the composition of each peak, to a very tight standard deviation (see Figures 3 and 10 for a visual representation, and Table 3 for the numerical values) we find that most planets in the first peak ($\sim 1.3R_\oplus$) are rocky and without a primordial atmosphere, which agrees with the results from Owen & Wu (2013, 2017), Jin & Mordasini (2018), and Swain et al. (2019). Conversely, we find that most planets in the second peak ($\sim 2.4R_\oplus$) have large primordial envelopes. Notwithstanding, there are exceptions such as Fe planets with small hydrogen atmospheres that could lay in the first peak or denuded $H_2O$ ice planets that have very low densities and therefore may lay in the second peak (Zeng et al. 2018) but these are very scarce. We believe that our predicted initial distribution of exoplanet radii (Figure 11) makes conceptual sense as most planets are born with large hydrogen depositories which results in their large puffy radii. Of these planets, very few have unusually small radii (i.e., small atmospheres) or unusually large radii (i.e., large atmospheres) which results in the initial distribution looking laplacian in nature.

One major difference between our paper and Owen & Wu (2017) is our predicted initial mass distributions of exoplanets. In their paper, their mass function follows a Rayleigh distribution with a mode at $3M_\oplus$. When we adopted the same distribution we were unable to generate the bimodal behavior with the right amplitudes at each peak (see Figure 15). This disparity is explained by the intrinsic nature of Rayleigh distributions, which generally produce a large number of values relatively close to zero. According to our simulations in order to achieve a distribution emulating the one by Fulton et al. (2017) it is necessary for there to be a deficiency in planets with small masses so a Rayleigh function is not appropriate. In addition, our best-fit initial mass distribution requires a lack of exoplanets with masses $\gtrsim 8M_\oplus$. According to our simulations, this lack of Neptunian-mass bodies is independent of stellar XUV irradiation. This drop in the occurrence rate of larger mass exoplanets is consistent with observations (e.g., Howard et al. 2010; Marcy et al. 2014; Malhotra 2015). In addition, a paucity in exoplanet masses beyond $\sim 10M_\oplus$ has been predicted by several planetary formation models (e.g., Ida & Lin 2004, 2005, 2008; Mordasini et al. 2009) as at this critical size efficient accretion of materials results in few bodies having intermediate masses between 10 and $100M_\oplus$. Concerning the flat distribution between 3 and $8M_\oplus$, this was not mandatory for a bimodal distribution in the radii, but it gave us a better fit than our best-fit truncated Gaussian function (see Figure 15). There are several processes that could give rise to this result. One potential explanation is that even though small cores are more common than larger ones (e.g., Schlichting et al. 2013; Simon et al. 2016), they are also harder to detect. Planets with smaller masses not only accrete less primordial gas (e.g., Stevenson 1999; Ikoma & Hori 2012; Chachan & Stevenson 2018), but they are also more susceptible

to atmospheric destruction. In addition, they are also more likely to be ejected from their planetary systems because of gravitational perturbations. This is particularly true if giant planets are present in the system, with simulations predicting that on average each star ejects ∼7.9 planets, of which ∼2.5 are terrestrial in size (Barclay et al. 2017). Although the exact demographics of rogue planets are a subject of dispute, it is generally accepted that there are at least billions in the Milky Way galaxy (e.g., Chambers & Wetherill 1998; Levison et al. 1998; Debes & Sigurdsson 2007). Furthermore, at very close distances to the host star (i.e., $\lesssim$1 au) there is a scarcity of solids, which limits the growth of planetesimals (e.g., Lodders 2003; Mordasini et al. 2009). Consequently, most seed embryos can only form beyond the ice line (e.g., Podolak & Zucker 2004; Martin & Livio 2012; D'Angelo & Podolak 2015). However, fast type 1 migration means that the depletion in planets with $3M_\oplus \lesssim M_P \lesssim 10M_\oplus$ disappears because bodies initially orbiting farther out move inwards (Mordasini et al. 2009). This implies that super-Earths and sub-Neptunes with masses $\lesssim 3M_\oplus$ would be preferentially depleted in comparison with heavier mass bodies. Since this reduction is mostly prevalent at shorter distances and we have an observational bias toward close-orbiting exoplanets; this decrease should be more pronounced. It is therefore possible that for smaller exoplanets; detection biases, more efficient ejections, and their predicted lack of fast type 1 migration could cancel out with their intrinsically larger populations, which results in a perceived initial flat mass function. Despite our initial mass function differing from Owen & Wu (2017), we predict an almost identical distribution to Ginzburg et al. (2018) even though their mass-loss mechanism is considerably different to ours. Their model argues for a broken power law that is flat from 0 to $5M_\oplus$ and then approaches zero for cores $>5M_\oplus$. We predict a slightly extended flat region, but the overall shape is in strong agreement.

With regards to our final mass function, it grows rapidly for smaller masses which is compatible with the observations from Howard et al. (2010). The rise in the abundance for bodies with $\lesssim 3M_\oplus$ is due to a collection of planets without hydrogen envelopes located in that region. Furthermore, the small maximum at $\sim 8M_\oplus$ is consistent with the observed mass peak of the *Kepler* planets, as shown by Marcy et al. (2014) and Malhotra (2015). However, even though the observed mass distribution is in agreement with our model, we are aware that the actual mass distribution of *Kepler* planets has not been reliably determined due to the difficulty of obtaining the masses of small exoplanets.

In Figure 15 we show how the final radius and mass distribution would change depending on our initial mass function. Our simulations show that the best-fit curve is a flat region from 3 to $8M_\oplus$ followed by a pareto distribution, as shown in Figure 13. The truncated Gaussian mass function shown in Figure 15 provides a possible alternative to our model, especially because the observations by Fulton et al. (2017) have considerable uncertainties. However, we found that the major problem with a truncated Gaussian function was the shape of the tail in relation to the position of the second radius peak. We were unable to get a fit where the location of the second peak lay at $\sim 2.4R_\oplus$ while at the same time matching the shape of the tail of the distribution. We also tried to fit a truncated laplace distribution (not shown in the manuscript) to the initial masses but our results were similar (albeit slightly worse) to the truncated Gaussian distribution. Finally, we show that without a deficiency in the occurrence rate at larger masses (i.e., $\gtrsim 8M_\oplus$), the bimodal distribution is strongly distorted and does not match the observations by Fulton et al. (2017).

### 5.1. Limitations of Our Model

When dealing with studies that are deeply theoretical such as this one it is crucial to consider the initial parameters and assumptions made since they can greatly affect the results. Due to the bimodal distribution of exoplanet radii being a multivariate phenomenon with a deeply stochastic nature it is not possible to test every parameter combination so assumptions were inevitable. One such assumption was that exoplanet orbital distances did not evolve and therefore remained constant. This is certainly false since many different effects can lead to large scale planetary migration, such as (and not limited to):

1. Gravitational scattering due to overdensities caused by other planets in the vicinity (e.g., Hansen & Zink 2015).
2. In a binary system or when there are two planets with different inclinations, the Kozai mechanism can cause the planet in question to exchange eccentricity and inclination resulting in tidal friction and a subsequent shrinking of the orbital distance (e.g., Kozai 1962; Nagasawa et al. 2008; Naoz et al. 2011).
3. Tidal migration. For example, a planet orbiting very close to its host star may induce a bulge which could lead to a loss in angular momentum if the star rotates faster than the planet's orbital period (e.g., Jackson et al. 2008; Penev & Sasselov 2010, 2011).

Points 1 and 2 normally occur rapidly ($\ll$1 Gyr) while 3 occurs on a longer timescale (∼*few* Gyr). Other aspects we ignored include, but are not limited to: how for close-orbiting tidally locked super-Earths, the tidal forces, together with the orbital and rotational centrifugal forces, could partially confine a hydrogen-rich atmosphere on the nightside (Modirrousta-Galian et al. 2020); secondary atmospheres and how they affect the radii of exoplanets; meteorite impacts and how they can influence atmospheres (e.g., Miller-Ricci et al. 2009; Lupu et al. 2014); star mergers forming disks from which planets can form (e.g., Tutukov 1991; Martin et al. 2011); and planet–planet collisions (e.g., Ji et al. 2011; Chrenko et al. 2018). These mechanisms are not only very hard to model, but most probably negligible and/or statistically insignificant.

## 6. Conclusions

After exposing $10^6$ synthetic exoplanets to their host star's XUV irradiation we show that the bimodal distribution observed by Fulton et al. (2017) can be reproduced. Our results indicate that for the radius gap to exist it is essential for there to be an initial paucity of exoplanets with masses $\gtrsim 8M_\oplus$. Furthermore, our best-fit results suggest that there is a flat distribution of exoplanets with masses 3–$8M_\oplus$ and a paucity for planets with masses $\lesssim 3M_\oplus$. In other words, the initial distribution of exoplanet masses, has a a great influence on the final radius distribution. With regards to the properties of the radius distribution, we predict that the peak situated at $\sim 1.3R_\oplus$ consists mostly of rocky denuded bodies while the maximum at $\sim 2.4R_\oplus$ marks a region full of hydrogen-rich exoplanets with a few mega-Earths. There are some very rare exceptions such as metallic planets with small hydrogen

atmospheres and denuded $H_2O$ ice planets (Zeng et al. 2018) which could lay in the first and second peak, respectively. Finally, we believe that our predictions can be tested in the not too distant future due to rapid technological advances. For instance, the *James Webb Space Telescope*, Atmospheric Remote-sensing Infrared Exoplanet Large-survey (ARIEL), Thirty Meter Telescope, and Extremely Large Telescope should become active in the next few years which would allow for far superior exoplanet observations. In the future, statistical methods on large data sets could be used in contrast to analyzing individual cases like at the present. For instance, with Tier 1 of ARIEL we could test the exoplanets at each peak on whether or not they have an atmosphere; this would provide strong evidence for or against our results. Furthermore, if we can get more unbiased mass distribution measurements for super-Earths and sub-Neptunes through Earth-based observations, this would be a strong test for the validity of our model.

We acknowledge the support of the ARIEL ASI-INAF agreement n.2018-22-HH.0. We thank P. Neague and the anonymous referee for their useful comments.

## References

Aggarwal, H. R., & Oberbeck, V. R. 1974, ApJ, 191, 577
Barclay, T., Quintana, E. V., Raymond, S. N., & Penny, M. T. 2017, ApJ, 841, 86
Becker, A., Lorenzen, W., Fortney, J. J., et al. 2014, ApJS, 215, 21
Chabrier, G., Saumon, D., Hubbard, W. B., & Lunine, J. I. 1992, ApJ, 391, 817
Chachan, Y., & Stevenson, D. J. 2018, ApJ, 854, 21
Chambers, J. E., & Wetherill, G. W. 1998, Icar, 136, 304
Chrenko, O., Brož, M., & Nesvorný, D. 2018, ApJ, 868, 145
D'Angelo, G., & Podolak, M. 2015, ApJ, 806, 203
Debes, J. H., & Sigurdsson, S. 2007, ApJL, 668, L167
Ehrenreich, D., & Désert, J.-M. 2011, A&A, 529, A136
Erkaev, N. V., Kulikov, Y. N., Lammer, H., et al. 2007, A&A, 472, 329
Espinoza, N., Brahm, R., Jordán, A., et al. 2016, ApJ, 830, 43
Fulton, B. J., Petigura, E. A., Howard, A. W., et al. 2017, AJ, 154, 109
Ginzburg, S., Schlichting, H. E., & Sari, R. 2016, ApJ, 825, 29
Ginzburg, S., Schlichting, H. E., & Sari, R. 2018, MNRAS, 476, 759
Gudkova, T. V., & Zharkov, V. N. 1999, P&SS, 47, 1201
Guillot, T. 1999, P&SS, 47, 1183
Guillot, T., Gautier, D., & Hubbard, W. B. 1997, Icar, 130, 534
Gupta, A., & Schlichting, H. E. 2018, MNRAS, 487, 24
Hansen, B. M. S., & Zink, J. 2015, MNRAS, 450, 4505
Hayashi, C., Nakazawa, K., & Nakagawa, Y. 1985, in Protostars and Planets II, ed. D. C. Black & M. S. Matthews (Tucson, AZ: Univ. Arizona Press), 1100
Howard, A. W., Marcy, G. W., Johnson, J. A., et al. 2010, Sci, 330, 653
Hubbard, W. B., & Marley, M. S. 1989, Icar, 78, 102
Ida, S., & Lin, D. N. C. 2004, ApJ, 604, 388
Ida, S., & Lin, D. N. C. 2005, ApJ, 626, 1045
Ida, S., & Lin, D. N. C. 2008, ApJ, 685, 584
Ikoma, M., & Hori, Y. 2012, ApJ, 753, 66
Jackson, B., Greenberg, R., & Barnes, R. 2008, ApJ, 681, 1631
Ji, J., Jin, S., & Tinney, C. G. 2011, ApJL, 727, L5
Jin, S., & Mordasini, C. 2018, ApJ, 853, 163
Jin, S., Mordasini, C., Parmentier, V., et al. 2014, ApJ, 795, 65
Kozai, Y. 1962, AJ, 67, 591
Kubyshkina, D., Fossati, L., Erkaev, N. V., et al. 2018a, A&A, 619, A151
Kubyshkina, D., Fossati, L., Erkaev, N. V., et al. 2018b, ApJL, 866, L18
Lammer, H., Erkaev, N. V., Odert, P., et al. 2013, MNRAS, 430, 1247
Lecavelier Des Etangs, A. 2007, A&A, 461, 1185
Levison, H. F., Lissauer, J. J., & Duncan, M. J. 1998, AJ, 116, 1998
Locci, D., Cecchi-Pestellini, C., & Micela, G. 2019, A&A, 624, A101
Lodders, K. 2003, ApJ, 591, 1220
Lupu, R. E., Zahnle, K., Marley, M. S., et al. 2014, ApJ, 784, 27
Malhotra, R. 2015, ApJ, 808, 71
Marcy, G. W., Isaacson, H., Howard, A. W., et al. 2014, ApJS, 210, 20
Martin, E. L., Spruit, H. C., & Tata, R. 2011, A&A, 535, A50
Martin, R. G., & Livio, M. 2012, MNRAS, 425, L6
Miller-Ricci, E., Meyer, M. R., Seager, S., & Elkins-Tanton, L. 2009, ApJ, 704, 770
Mizuno, H. 1980, PThPh, 64, 544
Mocquet, A., Grasset, O., & Sotin, C. 2014, RSPTA, 372, 20130164
Modirrousta-Galian, D., Locci, D., Tinetti, G., & Micela, G. 2020, ApJ, 888, 87
Moll, R., Garaud, P., Mankovich, C., & Fortney, J. J. 2017, ApJ, 849, 24
Mordasini, C., Alibert, Y., & Benz, W. 2009, A&A, 501, 1139
Nagasawa, M., Ida, S., & Bessho, T. 2008, ApJ, 678, 498
Naoz, S., Farr, W. M., Lithwick, Y., Rasio, F. A., & Teyssandier, J. 2011, Natur, 473, 187
Owen, J. E., & Lai, D. 2018, MNRAS, 479, 5012
Owen, J. E., & Wu, Y. 2013, ApJ, 775, 105
Owen, J. E., & Wu, Y. 2017, ApJ, 847, 29
Penev, K., & Sasselov, D. 2011, ApJ, 731, 67
Penev, K., & Sasselov, D. D. 2010, AAS Meeting Abstracts, 215, 328
Penz, T., & Micela, G. 2008, A&A, 479, 579
Penz, T., Micela, G., & Lammer, H. 2008, A&A, 477, 309
Podolak, M., & Zucker, S. 2004, M&PS, 39, 1859
Sanz-Forcada, J., Micela, G., Ribas, I., et al. 2011, A&A, 532, A6
Schlichting, H. E., Fuentes, C. I., & Trilling, D. E. 2013, AJ, 146, 36
Shibata, S., & Ikoma, M. 2019, MNRAS, 487, 4510
Shiraishi, M., & Ida, S. 2008, ApJ, 684, 1416
Siess, L., Dufour, E., & Forestini, M. 2000, A&A, 358, 593
Simon, J. B., Armitage, P. J., Li, R., & Youdin, A. N. 2016, ApJ, 822, 55
Sinukoff, E., Howard, A. W., Petigura, E. A., et al. 2017, AJ, 153, 271
Stevenson, D. J. 1982, P&SS, 30, 755
Stevenson, D. J. 1999, Natur, 400, 32
Swain, M. R., Estrela, R., Sotin, C., Roudier, G. M., & Zellem, R. T. 2019, ApJ, 881, 117
Tutukov, A. V. 1991, AZh, 68, 837
Wahl, S. M., Hubbard, W. B., Militzer, B., et al. 2017, GeoRL, 44, 4649
Watson, A. J., Donahue, T. M., & Walker, J. C. G. 1981, Icar, 48, 150
Zeng, L., Jacobsen, S. B., Sasselov, D. D., et al. 2018, AGUFM 2018, P53C-2985
Zeng, L., & Sasselov, D. 2013, PASP, 125, 227
Zeng, L., Sasselov, D. D., & Jacobsen, S. B. 2016, ApJ, 819, 127